CHINESE OPTICS LETTERS

Vol. 22, No. 5 | May 2024

Metalens with tilted structures for high-efficiency focusing at large-angle incidences

Yue Wang (王 月), Chen Chen (陈 晨)*, Shengjie Wu (吴圣杰), Xin Ye (叶 欣), Shining Zhu (祝世宁), and Tao Li (李 涛)**

National Laboratory of Solid State Microstructures, Key Laboratory of Intelligent Optical Sensing and Manipulations, Jiangsu Key Laboratory of Artificial Functional Materials, College of Engineering and Applied Sciences, Nanjing University, Nanjing 210093, China

*Corresponding author: chenchen2021@nju.edu.cn

**Corresponding author: taoli@nju.edu.cn

Received November 22, 2023 | Accepted January 24, 2024 | Posted Online May 14, 2024

The metalens has attracted remarkable attention due to its ultra-thin and ultra-light characteristics, which indicate great potential for compact imaging. However, the limited efficiency at a large angle incidence severely hinders the application of wide-angle focusing and imaging, which is pursued in the fast-developing imaging systems. Therefore, new strategies to improve the lens performance at large incident angles are in demand. In this work, we propose tilted structures for large-angle focusing with improved efficiency. Metalenses based on dynamic phase and geometric phase are designed and systematically characterized by numerical simulations. We show that tilted structures of unit cells significantly improve the lens performance at oblique incidences. In detail, the focusing efficiency of the metalens with tilted structures is increased over 25% at 30° incidence, as well as the modulation transfer function. In addition, we develop a hybrid metalens array achieving highly efficient wide-angle imaging up to 120°. We believe this design provides a feasible route toward wide-field and high-performance imaging applications.

Keywords: metalenses; tilted structures; large-angle incidence; high efficiency.

DOI: 10.3788/COL202422.053601

1. Introduction

It is of great significance to expand the field-of-view (FOV) in the entire imaging field. The conventional way to expand FOV is utilizing multiple refractive lenses, which makes the system bulky and heavy. Metalens[1-8], as a focusing phase designed metasurface[9-16], features ultra-thin and ultra-light advantages, and holds great potential for compact and miniaturized imaging systems. However, due to the limited FOV of each metalens, the realization of wide-angle imaging has been hindered. Recently remarkable efforts have been made to achieve wide FOV imaging[17-32], such as topology-optimized multilayered metalenses[18], quadratic metalenses[19], metalens doublets[20,21], and hybrid metalenses[22], while these designs are complex and usually need to sacrifice in certain aspects of imaging performance (e.g., degraded focusing quality, decreased entrance pupil). Recently researchers[25] developed a metalens array to compose an array-based camera and obtained a 120°-wide viewing angle. This work optimizes the phase by introducing a tilted phase design, but only solves the problem of focusing phase matching. However, for a metalens with only a kind of nanopillar structure, e.g., normal structures perpendicular to the substrate, in addition to the aberration caused by phase at large incident angles, there inevitably exist efficiency decreases as incident angle increases. Therefore, to meet the requirement of high-performance imaging at large angle incidence, new designs are highly demanded to improve the lens efficiency at oblique incidences.

In this work, we propose a tilted structure of unit cell for the metalens design, which can efficiently improve the focusing efficiency at oblique light incidences. The tilted structure, which breaks the symmetry of the z-axis, is equivalent to a tilted dipole[33-36]; thus, its strongest radiation lobe is tilted. Therefore, the focusing efficiency along the optical axis could be improved. In this work, proper focusing phase with respect to the incident light is introduced to each lens to correct aberrations. Then we systematically compare the focusing performances between the tilted design and the normal one with different incident angles, which is characterized by the transmission, diffraction efficiency, total efficiency, and corresponding modulation transfer function (MTF). Furthermore, we develop a hybrid metalens array consisting of tilted lenses and normal ones, which has higher imaging performance than the normal metalens array. Our results would pave the way to realize high-performance optical imaging devices in different scenarios.

2. Design and Characterization of Metalenses with Tilted Structures for Wide-Angle Focusing

2.1. Design principle

For a normally incident light, the ideal hyperbolic phase profile of a focusing metalens is expressed as

$$\phi(x,y) = k\left(f - \sqrt{x^2 + y^2 + f^2}\right), \tag{1}$$

where x and y are the coordinates along the metalens plane, $k = 2\pi/\lambda$ is the wavenumber at the design wavelength of λ, and f is the focal length. Such a phase distribution can focus light under paraxial illumination; however, it introduces severe aberrations in cases of oblique incidence. Therefore, we need to redesign the phase to eliminate the aberrations. The scheme is depicted in Fig. 1(a). The green and red lines indicate ray-I and ray-II with incident angle θ starting from the same wavefront of the incident plane wave and ending at the same focal spot on the focal plane.

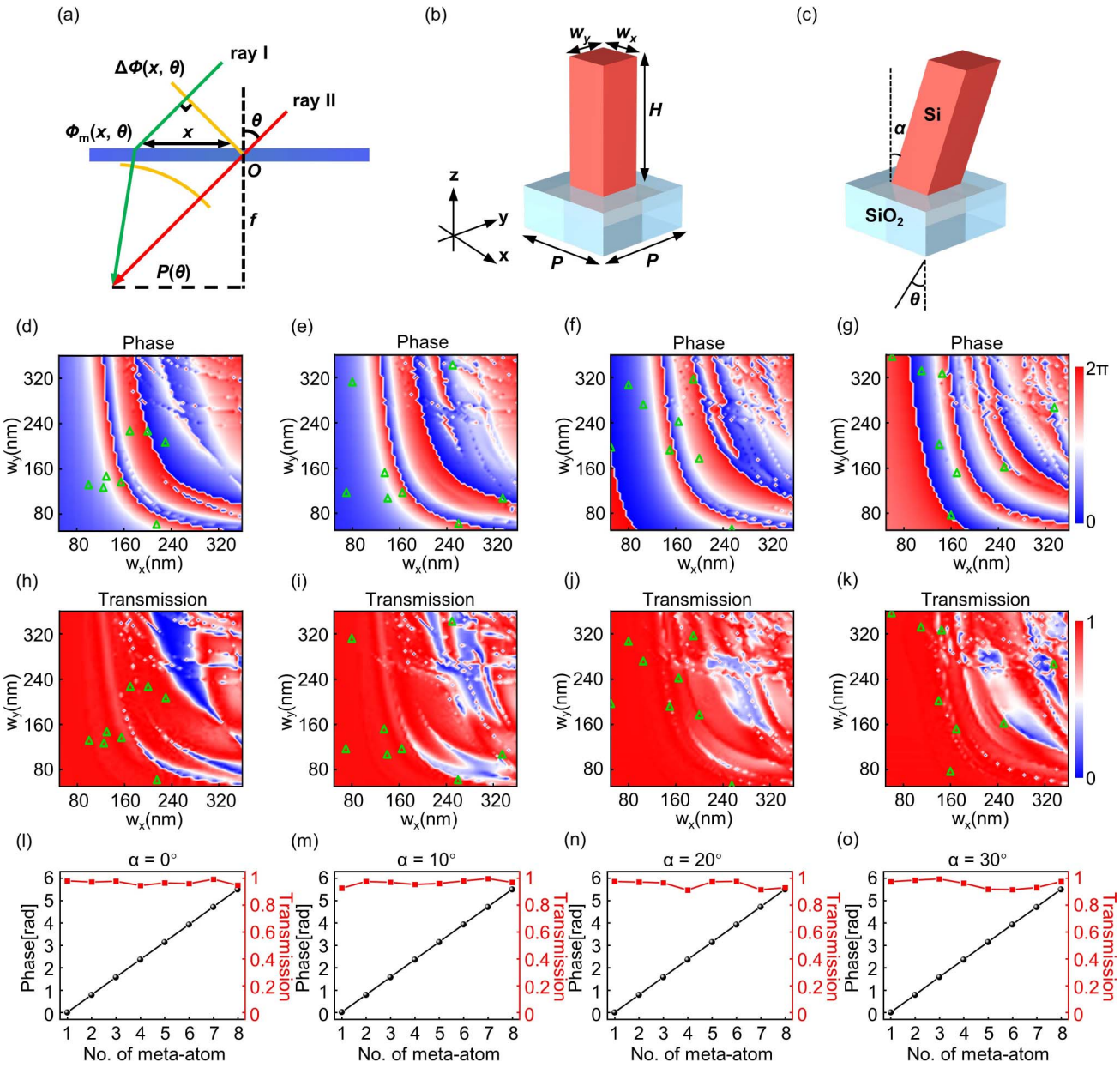

Fig. 1. Metalens design. (a) Schematic illustration of a metalens that converts a plane wave with an oblique angle θ into a spherical wave, which is focused into a focal point in the focal plane at a distance of $P(\theta)$ away from origin O. Tilt view of (b) a normal structure with $\alpha = 0°$ and (c) a tilted structure on the SiO_2 substate. Simulated (d)–(g) phase and (h)–(k) transmission of the structures of 50 nm $\leq w_x \leq$ 360 nm, 50 nm $\leq w_y \leq$ 360 nm at $\lambda = 850$ nm, of which α and θ are the same, with values of 0°, 10°, 20°, 30°, respectively. Green triangle marks: selected structures used in this work. (l)–(o) Phase (black circle markers) and transmittance (red square markers) of the chosen eight different structural parameters, of which the phase can cover 0–2π and transmission is all above 0.9.

Ray-II directly passes through the lens center, and the position of the focal point on the focal plane is at $P = f \tan\theta$, in which the lens can project an undistorted image on the image plane[37]. Ray-I reaches the lens at the position x. The phase delay between ray-I and ray-II at the interface is

$$\Delta\phi(x,\theta) = kx \sin\theta, \tag{2}$$

where θ is the incident angle in the air. Since the optical paths between the isophase surfaces (yellow lines) are equal, we can get the following relationship:

$$\Delta\phi(x,\theta) + \phi_m(x,y,\theta) + k\left[\sqrt{(f\tan\theta - x)^2 + y^2 + f^2} - f\right] = \text{const}. \tag{3}$$

By setting the constant to 0 and substituting Eq. (2) into Eq. (3), we can obtain the phase required by the metalens,

$$\phi_m(x,y,\theta) = k\left[f - \sqrt{(x - f\tan\theta)^2 + y^2 + f^2} - x\sin\theta\right]. \tag{4}$$

2.2. Metalenses designed in dynamic phase

The metalens can be designed in principles of dynamic phase[38-40] and geometric phase[41-43]. Here, we begin from the dynamic phase. The working wavelength is defined at 850 nm. The unit cell of the metalens consists of Si rectangle structures with length w_x, width w_y, height H, and tilted angle α on the SiO_2 substrate since Si has high refractive index and relatively low loss. Figure 1(b) shows a normal structure with $\alpha = 0°$, and the tilted structure is shown in Fig. 1(c). A commercial solution of Lumerical FDTD is employed in the optical simulations. The simulated phase and transmission maps are shown in Figs. 1(d)–1(k). The light is x-polarized, and the incident angle θ varies with respect to the tilted angle of α (e.g., $\theta = 0°$ when $\alpha = 0°$, and $\theta = 10°$ when $\alpha = 10°$). The length w_x and width w_y of the structure are swept from 50 nm to 360 nm with a step of 5 nm, height $H = 1$ μm, and period $P = 400$ nm. For the four different slanted structures, the phase can cover 2π, and the transmissions of most structures are close to unity. The green triangle marks indicate the selected 8 different structures, and the corresponding phase and transmission efficiency are shown in Figs. 1(l)–1(o). The average transmission efficiency of the 4 groups is 0.97, 0.97, 0.95, and 0.96, respectively.

Based on the selected structures, metalenses are designed with $\alpha = 0°$, 10°, 20°, 30° for the focusing analyses with incident angle θ ranging from −20° to 60°, respectively. All the structures of a metalens slant in the same direction and with a same angle of α. The lens size and focal length are $R = 7.4$ μm and $f = 35$ μm. The lens has a numerical aperture of 0.2. Figures 2(a)–2(d) show the corresponding light intensity distributions in the x–z plane (top) and x–y plane (bottom) for each metalens. It can be found that lenses with slanted structures show a brighter focus spot at oblique incidences. To better compare the metalens performance, the cross-sectional intensity distributions of focal spots in the x–y plane are shown in Figs. 2(e)–2(h). When $\alpha = 0°$, the focal spot energy shows maximal value at $\theta = 0°$ and decreases significantly with increasing θ, while as expected, when slanted angle α increases, the maximum peak shifts to the larger incident angle ($\theta > 0°$) cases.

Besides the focal spot intensity, we also quantify the transmission (T), diffraction efficiency (η_{dif}), and total efficiency (η_{tot}) of each lens, as shown in Figs. 3(a)–3(c). The η_{dif} is defined as $\eta_{dif} = I_{spot}/I_{plane}$, where I_{spot} is the total light intensity in the area with diameter $3\lambda/2\,\mathrm{NA}$ on the focal plane and I_{plane} is the total light intensity on the focal plane. The total efficiency η_{tot} is obtained by multiplying T and η_{dif}. For lenses with normal structures ($\alpha = 0°$), T is maximal at normal incidence ($T \sim 84.86\%$ at $\theta = 0°$) and drops with the increasing incident angle ($T \sim 68.79\%$ at $\theta = 30°$). Similarly, the diffraction efficiency decreases with increasing θ ($\eta_{dif} \sim 76.95\%$ at $\theta = 0°$, and $\eta_{dif} \sim 43.54\%$ at $\theta = 30°$). As a result, the total efficiency significantly degrades at oblique incidence ($\eta_{tot} \sim 65.29\%$ at $\theta = 0°$, and $\eta_{tot} \sim 29.95\%$ at $\theta = 30°$). However, we find that the lens performance at oblique incidence can be improved by utilizing the slanted structure. For example, η_{tot} of lens with $\alpha = 10°$, $\alpha = 20°$, and $\alpha = 30°$ at $\theta = 30°$ (51.31%, 56%, and 51.12%, respectively) are much higher than that of lenses with normal structures, which is attributed to the improved T and η_{dif}. The improvement of the efficiency can be explained as follows. The strongest radiation direction of the normal structure, which can be approximated as a dipole, is at $\theta = 0°$, and the transmission reaches its maximum. However, for the oblique incidences, the emission direction is not along the main lobe of the dipole, which results in the decrease of the efficiency. By tilting the structure, the equivalent main lobe of the dipole is rotated and redirects the maximum focusing. Therefore, the transmission of the tilted design is improved over the normal one. In addition, compared with normal structures, the shadow effect[44] of these slanted structures may be smaller under oblique incidence, which could also contribute to the improvement in T and η_{dif}. Figure 3(c) clearly shows the tendency of the efficiency maximum shifts to the larger incident angles. Our results indicate that the performance of the metalens can be improved at certain oblique incidences when the designed structure is tilted correspondingly with the incidence angle.

The MTF, characterizing the imaging performance of the lens, is also calculated, with the results shown in Figs. 3(d)–3(g), in which the diffraction limit (solid black line) is calculated by the focal spot of a plane wave passing through an ideal lens. For lenses with $\alpha = 0°$ [Fig. 3(d)], the MTF curve at $\theta = 0°$ is close to the diffraction limit. However, the focusing performance of the lens deteriorates as the angle increases; as a result, the MTFs at a large frequency drop away from the diffraction limit. The MTFs of the lens with $\alpha = 10°$, $\alpha = 20°$, and $\alpha = 30°$ at a large spatial frequency are obviously higher than that of the

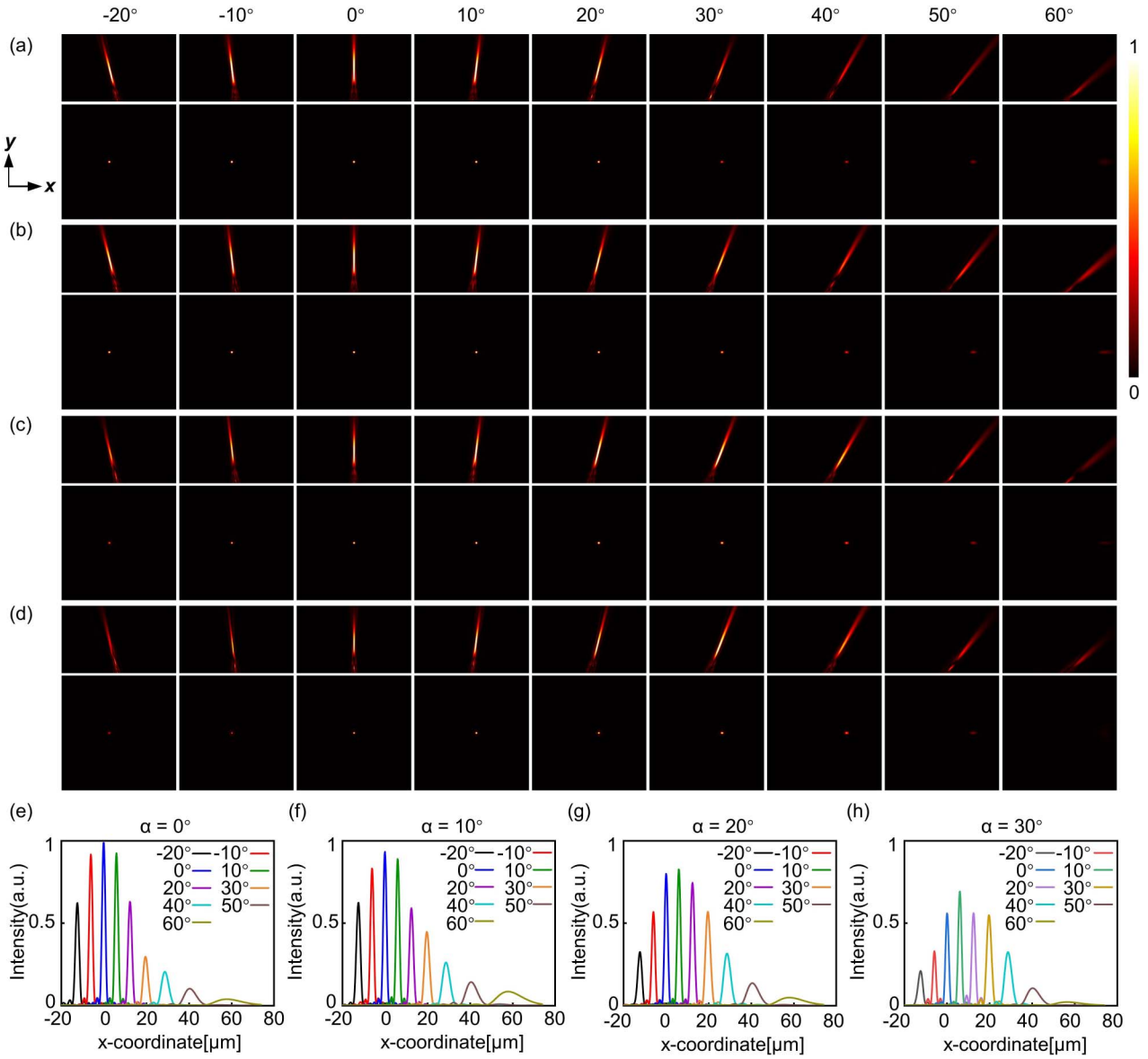

Fig. 2. Comparison of focal spots according to dynamic phase based metalenses with (a) $\alpha = 0°$, (b) $\alpha = 10°$, (c) $\alpha = 20°$, (d) $\alpha = 30°$ at incident angles of −20°, −10°, 0°, 10°, 20°, 30°, 40°, 50°, and 60°. The images at the top show the energy in the *x*–*z* plane. The images at the bottom show the energy in the focal (*x*–*y*) plane. (e)–(h) Cross-section view ($f = 35$ μm) of the intensity distribution along the *x*-direction shown in (a)–(d).

lens with $\alpha = 0°$, which indicates better focus performance of the lens with $\alpha = 10°$, $\alpha = 20°$, and $\alpha = 30°$ at large incident angle.

2.3. Metalenses designed in geometric phase

In addition, we design and characterize the metalens based on geometric phase. The w_x and w_y of the tilted structure ($\alpha = 20°$, $\theta = 20°$) are 115 nm and 305 nm, the corresponding transmittance is 92.16%, and the polarization conversion rate (PCR) is nearly 1. The R and f of the metalenses based on geometric phase are the same as that of metalenses based on dynamic phase. The cross-sectional intensity distributions of the focal spot in the *x*–*y* plane are shown in Figs. 4(a)–4(d). Compared to the lens with $\alpha = 0°$ shown in Fig. 4(a), the spot intensity of the lenses with $\alpha = 10°$, 20°, 30° [Figs. 4(b)–4(d)] improves at $\theta = 10°$ to $\theta = 60°$, which implies that lenses with tilted structures perform better at oblique incidence. Figures 4(e)–4(h) show T, η_{dif}, η_{tot}, and PCR of the lenses. The η_{dif} of all lenses with different α are similar under the same incident angle [Fig. 4(f)]. Notably, compared to the normal metalens, lenses with tilted structures show similar performance in PCR [Fig. 4(h)] but higher transmission [Fig. 4(e)] at oblique incidence, and thus exhibit higher total efficiency [Fig. 4(g)]. For example, η_{tot} of lens with $\alpha = 30°$ is increased by 17.98% at $\theta = 20°$ over the normal metalens. The improvement of total efficiency leads to better MTF at oblique incidences, as shown in Figs. 4(i)–4(l).

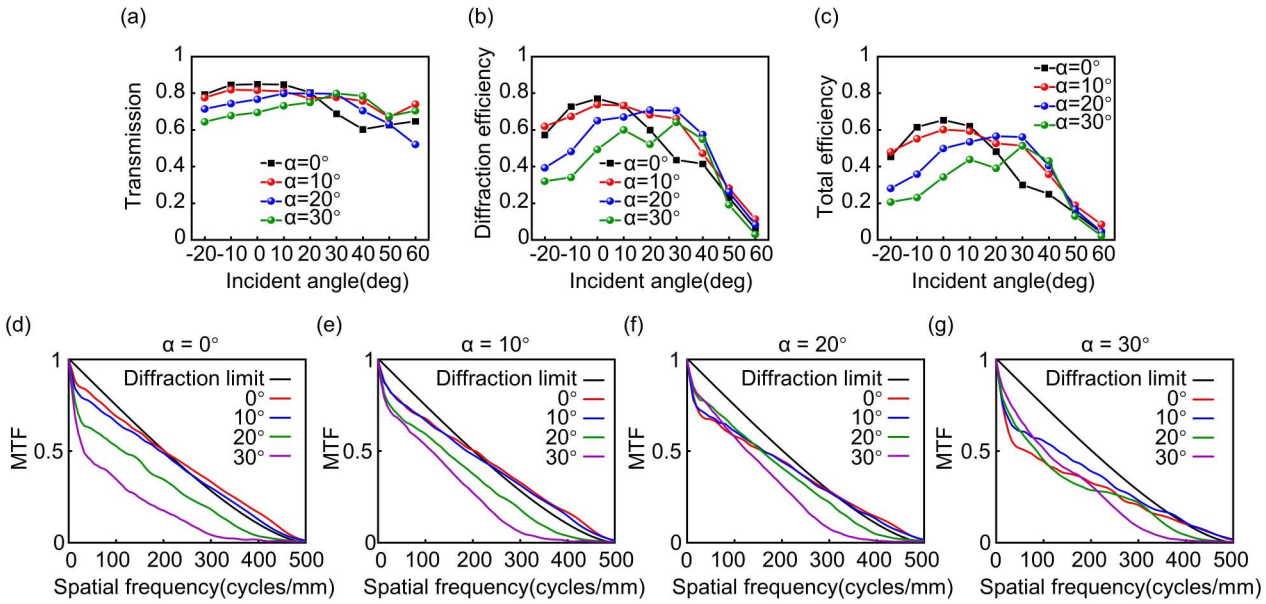

Fig. 3. Focusing performance of metalenses based on dynamic phase. Comparison of (a) transmission, (b) diffraction efficiency, and (c) total efficiency of the lens with four different α as a function of incident angle. Data points (rectangle mark) and data points (circular mark) represent $\alpha = 0°$ and $\alpha > 0°$, respectively, and the solid lines are eye guides. MTFs of the lens with (d) $\alpha = 0°$, (e) $\alpha = 10°$, (f) $\alpha = 20°$, (g) $\alpha = 30°$ in the sagittal plane.

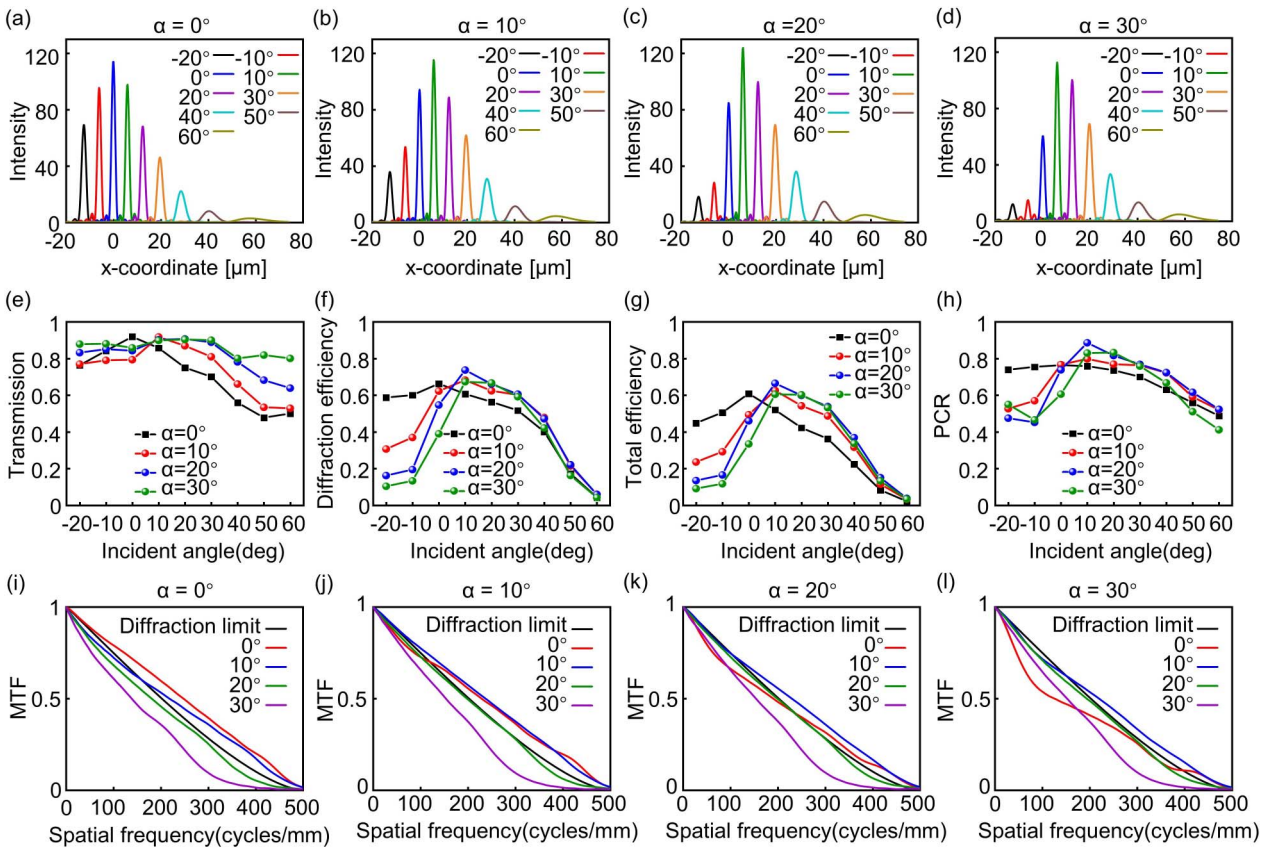

Fig. 4. Focusing results of metalenses based on geometric phase. (a)–(d) Cross-section view ($f = 35$ μm) of the intensity distribution along the x-direction. Comparison of (e) transmission, (f) diffraction efficiency, (g) total efficiency, and (h) PCR of the lens with four different α as a function of incident angle. Data points (rectangle mark) and data points (circular mark) represent $\alpha = 0°$ and $\alpha > 0°$, respectively, and the solid lines are eye guides. MTFs of the lens with (i) $\alpha = 0°$, (j) $\alpha = 10°$, (k) $\alpha = 20°$, (l) $\alpha = 30°$ in the sagittal plane.

3. Imaging Performance of the Wide-Angle Metalens Array

We first analyze the aberration of metalenses designed in different angles by Zemax software, as shown in Fig. 5(a). From bottom to the top the metalens is designed with respect to angles from 0° to 60°. From left to right are focal spots with incident angles from 0° to 60°. When the incident angles are close to the designed angles, the spots are small and have little aberrations, while the focal spots become much larger and show obvious coma aberrations when the deviation increases. We note that the spots smaller than 3 times of the Airy disk (black circle markers) have good focusing performance. We obtained the imaging range of each lens by analyzing the size of the focal spots, and it shows these lenses can cover an FOV of 60°, as shown in Fig. 5(b). In order to cover the angle of view of ±60°, we line up 13 metalenses with designed angles of 0°, ±10°, ±20°, ±30°, ±40°, ±50°, ±60° to form an array. The average total efficiency of the hybrid metalens array composed of normal and tilted metalenses is 13.59% higher than that of the normal metalens array only composed of normal metalenses, as shown in Fig. 5(c). Finally, we compare the images of objects composed of long letters such as "NANJINGUNIVERSITY" with the normal metalens array and the hybrid metalens array, respectively. The obtained sub-images at each angle can only show part of the letters, and by stitching these images together we can finally get the complete image, similar to the reported work[25]. Nevertheless, it can be seen that the hybrid metalens array presents a higher intensity image than the normal metalens array at large incidences (±20° to ±60°), as shown in Fig. 5(d), indicating the efficiency advantages of the hybrid lens array at large incident angles.

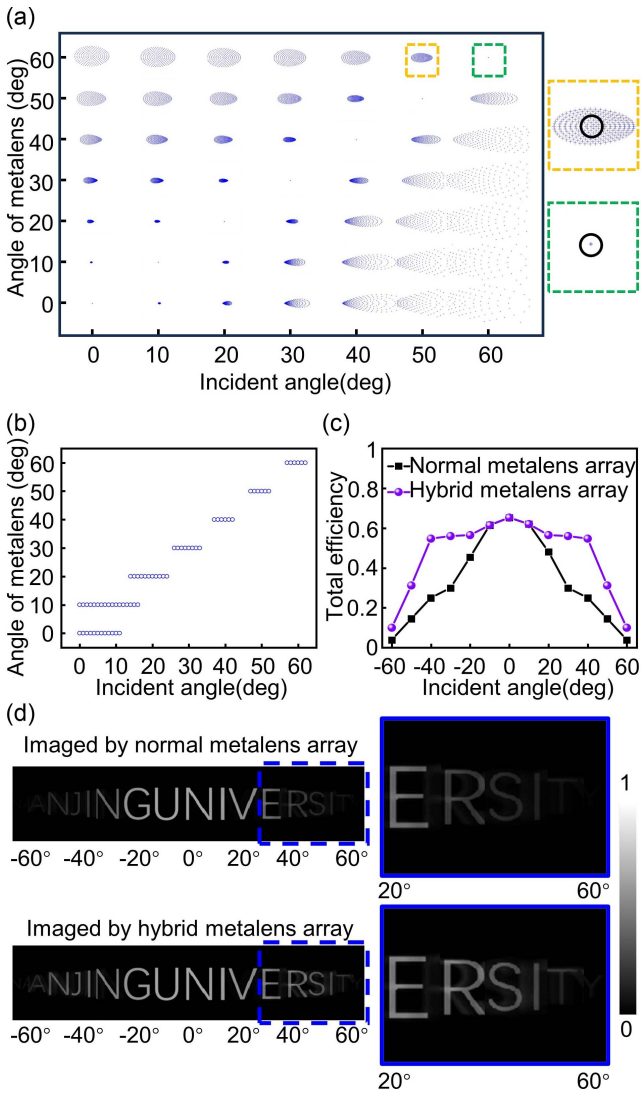

Fig. 5. (a) Focal spots of 7 metalenses with different design angles. (b) Imaging range of each lens in the metalens array. (c) Total efficiency of the normal metalens array and hybrid metalens array. (d) Wide-angle imaging of the normal metalens array and the hybrid metalens array. The two images on the right represent the enlarged image at the dashed line.

4. Conclusion

In summary, metalenses with tilted structures are systematically modeled and analyzed theoretically, which show better focusing performances under oblique incidences. Characterizations, including transmission, focusing efficiency, total efficiency, and MTF, of the lenses designed based on dynamic phase and geometric phase are investigated in detail. For dynamic phase, the total efficiency of the tilted design is improved by 26.05% over the normal lens at 30° incidence. As for geometric phase, the focus performance of the tilted design is also improved by 17.98% higher than the normal lens at 20° incidence. Compared with normal lenses, the significantly improved MTF curves demonstrate its superiority for oblique incidences. Moreover, the total efficiency of the tilted design based on dynamic phase and geometric phase slowly decreases about 9% and 7% as the angle of incidence varies from 0° to 30°, respectively. Finally, we propose a metalens array with 13 hybrid lenses and obtain a 120°-wide viewing angle with 13.59% higher average efficiency over the normal metalens array. We believe this design may provide some insights to high-efficiency meta devices related with wide angles in the future.

Acknowledgements

This work was supported by the National Key Research and Development Program of China (No. 2022YFA1404301) and National Natural Science Foundation of China (Nos. 62325504, 62305149, 92250304, and 62288101).

References

1. M. Khorasaninejad, W. Chen, R. C. Devlin, *et al.*, "Metalenses at visible wavelengths: diffraction-limited focusing and subwavelength resolution imaging," Science **352**, 1190 (2016).
2. C. Chen, W. Song, J.-W. Chen, *et al.*, "Spectral tomographic imaging with aplanatic metalens," Light Sci. Appl. **8**, 99 (2019).
3. X. Ye, X. Qian, Y. Chen, *et al.*, "Chip-scale metalens microscope for wide-field and depth-of-field imaging," Adv. Photonics **4**, 046006 (2022).

4. W. Zang, Q. Yuan, R. Chen, *et al.*, "Chromatic dispersion manipulation based on metalenses," Adv. Mater. **32**, 1904935 (2020).
5. W. Liu, H. Cheng, J. Tian, *et al.*, "Diffractive metalens: from fundamentals, practical applications to current trends," Adv. Phys. X **5**, 1742584 (2020).
6. S.-W. Moon, Y. Kim, G. Yoon, *et al.*, "Recent progress on ultrathin metalenses for flat optics," iScience **23**, 101877 (2020).
7. C. Chen, X. Ye, J. Sun, *et al.*, "Bifacial-metasurface-enabled pancake metalens with polarized space folding," Optica **9**, 1314 (2022).
8. P. Lalanne and P. Chavel, "Metalenses at visible wavelengths: past, present, perspectives," Laser Photonics Rev. **11**, 1600295 (2017).
9. N. Yu and F. Capasso, "Flat optics with designer metasurfaces," Nat. Mater. **13**, 139 (2014).
10. F. Capasso, "The future and promise of flat optics: a personal perspective," Nanophotonics **7**, 953 (2018).
11. F. Aieta, P. Genevet, M. A. Kats, *et al.*, "Aberration-free ultrathin flat lenses and axicons at telecom wavelengths based on plasmonic metasurfaces," Nano Lett. **12**, 4932 (2012).
12. S. M. Kamali, E. Arbabi, A. Arbabi, *et al.*, "Angle-multiplexed metasurfaces: encoding independent wavefronts in a single metasurface under different illumination angles," Phys. Rev. X **7**, 041056 (2017).
13. Z.-L. Deng, J. Deng, X. Zhuang, *et al.*, "Diatomic metasurface for vectorial holography," Nano Lett. **18**, 2885 (2018).
14. W. Chen, A. Y. Zhu, and F. Capasso, "Flat optics with dispersion-engineered metasurfaces," Nat. Rev. Mater. **5**, 604 (2020).
15. C. Chen, S. Gao, X. Xiao, *et al.*, "Highly efficient metasurface quarter-wave plate with wave front engineering," Adv. Photonics Res. **2**, 2000154 (2021).
16. C. Chen, S. Gao, W. Song, *et al.*, "Metasurfaces with planar chiral meta-atoms for spin light manipulation," Nano Lett. **21**, 1815 (2021).
17. X. Luo, F. Zhang, M. Pu, *et al.*, "Recent advances of wide-angle metalenses: principle, design, and applications," Nanophotonics **11**, 1 (2022).
18. Z. Lin, B. Groever, F. Capasso, *et al.*, "Topology-optimized multilayered metaoptics," Phys. Rev. Appl. **9**, 044030 (2018).
19. E. Lassalle, T. W. W. Mass, D. Eschimese, *et al.*, "Imaging properties of large field-of-view quadratic metalenses and their applications to fingerprint detection," ACS Photonics **8**, 1457 (2021).
20. A. Arbabi, E. Arbabi, S. M. Kamali, *et al.*, "Miniature optical planar camera based on a wide-angle metasurface doublet corrected for monochromatic aberrations," Nat. Commun. **7**, 13682 (2016).
21. B. Groever, W. Chen, and F. Capasso, "Meta-lens doublet in the visible region," Nano Lett. **17**, 4902 (2017).
22. M. Kang, Y. Ra'di, D. Farfan, *et al.*, "Efficient focusing with large numerical aperture using a hybrid metalens," Phys. Rev. Appl. **13**, 044016 (2020).
23. T. Li, C. Chen, X. Xiao, *et al.*, "Revolutionary meta-imaging: from superlens to metalens," Photon. Insights **2**, R01 (2023).
24. M. Y. Shalaginov, S. An, F. Yang, *et al.*, "Single-element diffraction-limited fisheye metalens," Nano Lett. **20**, 7429 (2020).
25. J. Chen, X. Ye, S. Gao, *et al.*, "Planar wide-angle-imaging camera enabled by metalens array," Optica **9**, 431 (2022).
26. A. Martins, K. Li, J. Li, *et al.*, "On Metalenses with arbitrarily wide field of view," ACS Photonics **7**, 2073 (2020).
27. F. Zhang, M. Pu, X. Li, *et al.*, "Extreme-angle silicon infrared optics enabled by streamlined surfaces," Adv. Mater. **33**, 2008157 (2021).
28. M. Pu, X. Li, Y. Guo, *et al.*, "Nanoapertures with ordered rotations: symmetry transformation and wide-angle flat lensing," Opt. Express **25**, 31471 (2017).
29. J. Engelberg, C. Zhou, N. Mazurski, *et al.*, "Near-IR wide-field-of-view Huygens metalens for outdoor imaging applications," Nanophotonics **9**, 361 (2020).
30. C. Hao, S. Gao, Q. Ruan, *et al.*, "Single-layer aberration-compensated flat lens for robust wide-angle imaging," Laser Photonics Rev. **14**, 2000017 (2020).
31. F. Yang, M. Y. Shalaginov, H.-I. Lin, *et al.*, "Wide field-of-view metalens: a tutorial," Adv. Photonics **5**, 033001 (2023).
32. H. Liang, A. Martins, B.-H. V. Borges, *et al.*, "High performance metalenses: numerical aperture, aberrations, chromaticity, and trade-offs," Optica **6**, 1461 (2019).
33. X. Wang, C. Dai, X. Yao, *et al.*, "Asymmetric angular dependence for multicolor display based on plasmonic inclined-nanopillar array," Nanoscale **13**, 7273 (2021).
34. N. Kim, M. Kim, J. Jung, *et al.*, "Highly angle-sensitive and efficient optical metasurfaces with broken mirror symmetry," Nanophotonics **12**, 2347 (2023).
35. Y. Chen, H. Deng, X. Sha, *et al.*, "Observation of intrinsic chiral bound states in the continuum," Nature **613**, 474 (2023).
36. X. Zhang, Y. Liu, J. Han, *et al.*, "Chiral emission from resonant metasurfaces," Science **377**, 1215 (2022).
37. A. Kalvach and Z. Szabó, "Aberration-free flat lens design for a wide range of incident angles," J. Opt. Soc. Am. B **33**, A66 (2016).
38. M. Faraji-Dana, E. Arbabi, A. Arbabi, *et al.*, "Compact folded metasurface spectrometer," Nat. Commun. **9**, 4196 (2018).
39. A. Arbabi, Y. Horie, A. J. Ball, *et al.*, "Subwavelength-thick lenses with high numerical apertures and large efficiency based on high-contrast transmitarrays," Nat. Commun. **6**, 7069 (2015).
40. Z. Fan, Z. Shao, M. Xie, *et al.*, "Silicon nitride metalenses for close-to-one numerical aperture and wide-angle visible imaging," Phys. Rev. Appl. **10**, 014005 (2018).
41. L. Cong, N. Xu, W. Zhang, *et al.*, "Polarization control in terahertz metasurfaces with the lowest order rotational symmetry," Adv. Opt. Mat. **3**, 1176 (2015).
42. S. Jiang, X. Xiong, Y. Hu, *et al.*, "High-efficiency generation of circularly polarized light via symmetryinduced anomalous reflection," Phys. Rev. B **91**, 125421 (2015).
43. M. Kang, J. Chen, X. Wang, *et al.*, "Twisted vector field from an inhomogeneous and anisotropic metamaterial," J. Opt. Soc. Am. B **29**, 572 (2012).
44. M. S. L. Lee, P. Lalanne, J. C. Rodier, *et al.*, "Imaging with blazed-binary diffractive," J. Opt. A **4**, S119 (2002).